Quantitative in situ mapping of elements in deep-sea hydrothermal vents using laser-induced breakdown spectroscopy and multivariate analysis

Tomoko Takahashi[a,b,c], Soichi Yoshino[a], Yutaro Takaya[d,e,f,g], Tatsuo Nozaki[e,f,h,g], Koichi Ohki[i], Toshihiko Ohki[i], Tetsuo Sakka[j], Blair Thornton[a,k]

[a] *Institute of Industrial Science, The University of Tokyo, 4-6-1, Komaba, Meguro-ku, Tokyo 153-8505, Japan*
[b] *Advanced Science-Technology Research Program, Japan Agency for Marine-Earth Science and Technology, 2-15 Natsushima-cho, Yokosuka, Kanagawa 237-0061, Japan*
[c] *Department of Chemistry and the Institute for Life Sciences, University of Southampton, University Road, Southampton SO17 1BJ, UK*
[d] *School of Creative Science and Engineering, Waseda University, 3-4-1 Okubo, Shinjuku-ku, Tokyo 169-8555, Japan*
[e] *Submarine Resources Research Center, Research Institute for Marine Resources Utilization, Japan Agency for Marine-Earth Science and Technology, 2-15 Natsushima-cho, Yokosuka, Kanagawa 237-0061, Japan*
[f] *Frontier Research Center for Energy and Resources, The University of Tokyo, 7-3-1 Hongo, Bunkyo-ku, Tokyo 113-8656, Japan*
[g] *Ocean Resources Research Center for Next Generation, Chiba Institute of Technology, 2-17-1 Tsudanuma, Narashino, Chiba 275-0016, Japan*
[h] *Department of Planetology, Kobe University, 1-1 Rokkodai-cho, Nada-ku, Kobe, Hyogo 657-8501, Japan*
[i] *OK Lab. Co. Ltd., 8-7-3, Shimorenjyaku, Mitaka, Tokyo 181-0013, Japan*
[j] *Department of Energy and Hydrocarbon Chemistry, Graduate School of Engineering, Kyoto University, Nishikyo-ku, Kyoto 615-8510, Japan*
[k] *Centre for In situ and Remote Intelligent Sensing, Faculty of Engineering and Physical Science, University of Southampton, Burgess Road, Southampton SO16 7QF, UK*

Abstract

This study describes a method to quantify the chemical composition of deep-sea hydrothermal deposits in situ using laser-induced breakdown spectroscopy (LIBS). Partial least squares (PLS) regression analysis is applied to spectra obtained using a long laser pulse with a duration of 150 ns. The number of measurements needed to address the spatial heterogeneity of samples is determined through high-resolution mapping of the elemental distribution in rock samples. PLS applied to laboratory measured seawater-submerged samples achieved an average relative error (RE) of 25 % for Cu, Pb, and Zn compared to benchmark concentration values in cross-validation and validation studies, where both the benchmark concentration values and LIBS spectral data are made available with

this publication. The PLS model was applied to LIBS signals obtained in situ from hydrothermal deposits at 1000 m depth in the ocean. The results show that target inhomogeneity limits the accuracy of the surface LIBS measurements compared to benchmark values from bulk analysis of samples. Making multiple measurements with small position offsets at each location improves the accuracy of estimates compared to an equivalent number of measurements at a single position. Maps of element distribution generated using quantified in situ data demonstrates how chemical survey outputs can be generated by combining LIBS with multivariate analysis. This enables real-time chemical feedback during deep-sea operations and chemical surveys in situations or with platforms where sample recovery is not possible.

Keywords: Laser-induced breakdown spectroscopy (LIBS), In situ chemical analysis, Deep-sea explorations, Seafloor mineral resources, Multivariate analysis, Partial least squares regression analysis

1. Introduction

Accurately geo-referenced chemical information from analysis of rocks and deposits sampled using underwater robots has advanced our understanding of deep-sea geochemical processes (Thornton et al., 2015). Though seafloor mineral resources such as hydrothermal sulphide deposits are of interest from scientific and potential commercial perspectives, the time and cost of conventional sampling at depth of hundreds to thousands of metres and analysis in a laboratory are limiting. The number of samples that can be recovered using remotely operated vehicles (ROVs), grabs or dredges is limited to the capacity of each platform and typically feedback of chemical information requires long time. This combined with the non-uniform spatial distribution of elements means that most surveys become multi-expedition efforts. To address these limitations on land, in situ measurement techniques are often applied. These use portable X-ray fluorescence (XRF) or laser-induced breakdown spectroscopy (LIBS) prior to sampling or drilling to determine locations to efficiently characterise the site.

The aim of this work is to develop an equivalent method to quantify in situ measurements of deep-sea rocks and deposits using LIBS (Thornton et al., 2015), and demonstrate how this can be applied to data obtained at a 1000 m depth hydrothermal site.

LIBS is a form of atomic emission spectroscopy that analyses light emitted from atoms and ions of ablated material in a plasma created by focusing a high power laser pulse on a target. The advantages of LIBS are that it requires no sample preparation, the measurements are quick, the results are available in real-time, and a micro-scale depth profile can be obtained for solid samples. The technique has been applied to field measurements in various environments such as in nuclear power plants (Whitehouse et al., 2001) and on Mars (Wiens et al., 2012). While XRF and LIBS have comparable accuracy for quantitative analysis of solid targets (Rakovský et al., 2014), LIBS has the advantage that it can be used in bulk liquid environments. Though it is often reported that signal degradation is observed when targets are measured in water using a conventional laser pulse (Pichahchy et al., 1997, Giacomo et al., 2004, Lazic et al., 2005), several techniques have been described to address this limitation. Many groups have reported enhancement of signals from solids submerged in water by using a double-pulse technique (Nyga and Neu, 1993). However, the double-pulse method is sensitive to the external pressure (Giacomo et al., 2011, Takahashi et al., 2013), which does not allow us to use the LIBS technique in deep-sea environments. Lawrence-synder et al. (2006) were the first to observe well-resolved spectral lines of bulk ionic solutions at high pressures of up to 30 MPa using a conventional single pulse laser (Lawrence-Snyder et al., 2006), followed by further investigations by Michel et al. (2007, 2008) (Michel et al., 2007, Michel and Chave, 2008). Other groups also reported similar results for bulk solutions (Thornton et al., 2014, Hou et al., 2014), with Thornton et al. (2011) demonstrating measurement of solids at high pressure for the first time (Thornton and Ura, 2011). This led to in situ LIBS measurements of seawater and solid targets in the deep-sea for the first time in 2011 (Thornton et al., 2013b), with other groups following several years later (Guo et al., 2017). A

major development for underwater measurements was reported by using a laser pulse with a long duration of ≥ 100 ns yielding significant enhancements in signal quality for underwater samples (Sakka et al., 2006, 2007, 2009, 2014). This has been found to be applicable to both bulk liquids (Thornton et al., 2014) and submerged solids (Thornton et al., 2013a) at pressures of up to 30 MPa without significant signal degradation. In 2013, the long-pulse method was applied to in situ measurements of seawater and hydrothermal deposits at depths of more than 1000 m using "ChemiCam", a 3000 m depth rated deep-sea LIBS instrument. Spectra with a high enough resolution to detect the major elements in deep-sea minerals were successfully obtained, showing that major elements ratios could be accurately determined from in situ measurements to correctly classify deposits using ternary diagrams (Thornton et al., 2015).

The next step for deep-sea LIBS analysis is quantification of chemical compositions of rock samples. Generic methods to quantify field measurements of unknown targets with complex compositions in water have not yet been developed. Large shot-to-shot fluctuations of signals seen in underwater LIBS signals due to short plasma lifetime are problematic for quantitative analysis. Though quantitative analysis using calibration curves has been demonstrated with matrix-matched standards in air (Lazic et al., 2005), and for specific elements under controlled conditions (Matsumoto et al., 2015), quantitative analysis of samples with complex compositions is hampered by strong matrix effects. Calibration-free LIBS (CF-LIBS) cab be used to correct matrix effects and signal fluctuations through theoretical analysis of the spectrum (Ciucci et al., 1999). The compositions of Cu and Zn of brass alloys submerged in water were determined using CF-LIBS with relative errors (REs) of $\leq 10\,\%$ (Takahashi et al., 2015). However, to apply this method, the peaks of all elements contained in the target need to be observed, and this limits the application of CF-LIBS to geological samples with complex compositions and limited prior knowledge (Sallé et al., 2006, Herrera et al., 2009). Chemometrics methods such as multivariate analysis and artificial neural networks (ANNs) are promising tools for application to complex materials (Death et al., 2008, 2009, Sirven et al., 2006). Multivariate

analysis can separate noise from useful signals in spectra, making it robust to matrix effects by constructing a statistical model that relates latent variables (LVs) extracted from the full spectra of all samples in a database with their known compositions. Multivariate methods have been investigated for LIBS spectra of Martian rocks (Clegg et al., 2009). The accuracy obtained from partial least squares (PLS) regression analysis was shown to be robust compared to other multivariate methods in a benchmark study (Boucher et al., 2015), and it has been adopted to quantify in situ data obtained for Martian rocks (Maurice et al., 2016, Clegg et al., 2009). For underwater applications, while classification and identification of seawater-submerged rocks have been demonstrated (Yoshino et al., 2018, Yelameli et al., 2019), quantitative analysis has not previously been reported. When PLS was applied to LIBS spectra of water-submerged brass samples obtained using a long laser pulse, it was found that signal pre-processing methods such as normalisation and database segmentation by excitation temperature (Takahashi et al., 2016, 2018) improve accuracy. This study applies PLS to the spectra of 40 seawater-submerged pelletised deposit samples to characterise the accuracy of the method when measuring Cu, Pb and Zn concentrations, and subsequently to in situ measurements of hydrothermal deposits in the field at 1000 m water depth in the middle Okinawa Trough, Japan. The accuracy of the PLS analysis is evaluated and the method is applied to quantify field measurements made using different operational strategies, and a geo-referenced map of the major element composition of a deep-sea vent field is generated.

2. Measurement setup and materials

2.1. Experimental setup

2.1.1. Laboratory setup

The laboratory setup used to verify the accuracy of the method is described in our previous work (Yoshino et al., 2018). The plasma was generated on the seawater-submerged targets using a custom-built Q-switched Nd:YAG laser with

a wavelength of 1064 nm, pulse energy of 5 mJ, and pulse width of 150 ns. The repetition rate was 2 Hz and the laser beam was delivered via a 600 μm fused-silica fibre. This setup simulates the same conditions as in situ measurements with the exception of water pressure, which had been shown to have a negligible effect up to 30 MPa for long pulse measurements (Thornton et al., 2013a). The targets were submerged in the artificial seawater (Osakayakken. Co. Ltd., Marine Art SF-1) at a 10 mm distance from the face of a custom-made objective lens with 5 $\times$ magnification that was also submerged. The diameter of the laser beam at its focal point is 120 μm. The light emitted from the plasma passes through a custom-built spectrograph via a bundle of 43 fused-silica fibres with the 100 μm diameter each and the spectra are recorded using an intensified charged coupled device (ICCD, Princeton Instruments, PI-MAX 4) from 320 nm to 550 nm at a resolution of 0.25 nm. The high variability of underwater plasmas requires a high throughput so that well-resolved signals can be observed from a single shot. At the same time, a high resolution is needed to resolve the complex spectra obtained from underwater deposits. To satisfy both these conditions, ChemiCam uses a Czerny Turner spectrometer coupled to an ICCD camera, where a 320 to 550 nm range at 0.25 nm represents a good tradeoff between simplicity of materials in the optical setup, high throughput and resolution. Wavelength calibration was performed using a mercury calibration lamp (Ocean Optics, HG-1). The spectral sensitivity characteristics of the observation setup were calibrated using a standard halogen lamp (Ocean Optics, HD-2000-CAL). The gate width and the gate delay of the ICCD were set to 500 ns and 400 ns, respectively, as these values were found to achieve the largest signal-to-noise ratio.

2.1.2. In situ deep-sea LIBS device

The specification of ChemiCam is summarised in Table S1 (Supplementary Material). The main housing consists of a long-pulse laser, spectrograph, and ICCD with identified specifications in section 2.1.1. The central processing unit (CPU, Advantech Co., Ltd., PCM-3363 and PCM-3665) is located in the main

housing. The CPU controls the laser, ICCD and other components, and logs all data. Measurements and instrument settings are monitored in real-time via an RS232 serial or an Ethernet connection to the device. The laser pulse shape and intensities measured using photodiodes built within the device are stored for each pulse. The fibre cable is the same as laboratory setup and connected to the main housing, protected by a flexible, pressure resistance stainless steel pipe. A focusing probe of diameter 200 mm and length 500 mm is attached to the other end of the fibre. The device relies on the use of an ROV manipulator to bring the probe near the target. A single-axis linear stage with a stroke length of 40 mm and step resolution of 40 μm is used during in situ measurements for fine focusing. A guiding laser beam with a wavelength of 656 nm is delivered through one of bundled fibre cables, and the light intensity of the reflected beam is used for automatic focusing. While the focused points of the 656 nm guide and 1064 nm measurement lasers are different due to chromatic aberration, the difference is less than 0.1 % of total distance to the focal point, which can be considered negligible.

2.2. Materials

2.2.1. Samples for cross-validation and validation: bulk pellets

The samples used in this work are shown in Table S2 (Supplementary Material). Samples 1 to 40 were used for cross-validation and validation. Samples 1 to 5 are standard geological powder samples taken at sites on land, issued by Geochemical Reference Samples, National Institute of Advance Industrial Science and Technology, Japan. The other samples were collected at different deep-sea hydrothermal fields. Samples 6 to 10 and 12 to 40 are all sulphide-rich chimney and mound ore samples taken mostly from the Okinawa Trough, Japan, except for sample 10 that was taken at the Pika Site in the Southern Mariana Trough (12.9° N, 143.6° E), which is dominated by pyrite (FeS_2). Sample 11 is the only Ca-sulphate-rich chimney sample. Samples 9, 11, 13, 18 and 19 were taken at the Hatoma Knoll (24.86° N, 123.84° E), and sample 7 was taken at the Hakurei Site, Izena Hole (27.25° N, 127.07° E). The other samples were taken

at the Original Site, Iheya North Knoll (27.79° N, 126.90° E). The rock samples taken from the seafloor were crushed into powder using an agate mortar and sifted using a sieve with a 212 μm opening size in order to obtain pellets that are representative of bulk composition with less heterogeneity than the original samples. The compositions of rock samples taken from the seafloor, *i.e.* samples 6 to 54, were certified using other well established laboratory techniques to provide benchmark concentration values. Samples 6 to 23 were measured using inductively coupled plasma atomic emission spectroscopy (ICP-AES), inductively coupled plasma mass spectroscopy (ICP-MS), or instrumental neuron activation analysis (INAA) by Activation Laboratories Ltd. Samples 24 to 54 were measured using ICP-MS at the Japan Agency for Marin-Earth Science and Technology (JAMSTEC). Powder bulk pellets of samples 1 to 40 were used for LIBS measurements in the laboratory. Pellets were made using a hydraulic press (Specac, Atlas^{TM} 15 Ton Hydraulic Press) under a 10 tonne load for 5 minutes. The powder was put into a polyvinyl chloride ring of internal diameter 13 mm and 5 mm height (Rigaku, polyvinyl chloride ring for powder samples). This was sandwiched between pellet dies (Specac, Atlas^{TM} Evacuable Pellet Dies). The Cu concentrations of samples for cross-validation vary from 0.00 to 8.02 %, Pb concentrations vary from 0.00 to 26.5 %, and Zn concentrations vary from 0.00 to 51.2 %. The irradiation point was moved every 10 or 20 shots depending on sample mechanical properties to limit the irradiation damage.

Samples 24 to 54 were collected during in situ LIBS experiments. Details of in situ data acquisition are explained in section 2.2.2. Several rocks were collected at some of the locations, *e.g.* NB-6 (samples 29 and 30), to characterise handspecimen-scale inhomogeneity. Quantification results of in situ data were compared to the average composition of samples recovered at each location. The compositions of the samples determined using well established laboratory techniques in Table S2 and other minor elements are released as an open dataset together with their underwater LIBS spectra with this publication, accessible at https://github.com/ocean-perception/chemicam_open_database.

2.2.2. In situ data: rock surfaces

In situ data was collected at the Original Site, Iheya North Knoll at a water depth of 1000 m in the Okinawa Trough during the NT16-01 cruise of the research vessel (R/V) Natsushima in January, 2016, and KS-18-J03 of the R/V Shinseimaru in February, 2018. In both expeditions, ChemiCam was mounted on the ROV Hyper-Dolphin as shown in Fig. 1 (a). During operation, the ROV manipulator held the focusing probe as shown in Fig. 1 (b). A regional map of the Iheya North hydrothermal field, middle Okinawa Trough and bathymetry around the survey area are shown in Fig. 2 (a) and (b), respectively. The bathymetry in Fig. 2 was taken from the General Bathymetric Chart of the Oceans (The GEBCO_2019 Grid, 15 arc-second intervals). The bathymetry map in Fig. 2 (b) was produced by the autonomous underwater vehicle (AUV) Urashima survey during the cruise YK07-07 of R/V Yokosuka in May, 2007 (Yamamoto et al., 2009). The applied multi-narrow beam echo sounder was a SEABAT 7125 whose frequency and beam width were 400 kHz and 1.0 degree $\times$ 0.5 degree (fore-aft $\times$ athwart). The survey area is a large, active hydrothermal vent (Takai et al., 2012). A top view projection of a 3D visual reconstruction of the survey area and the corresponding hillshade map are shown in Fig. 2 (c) and (d), respectively (Thornton et al., 2016, Bodenmann et al., 2017a,b, 2013). The measurement locations shown in Fig. 2 were determined by matching visually the 3D image (Fig. 2 (c)), the real-time video image sent from the ROV, and the ROV's position information obtained using the super-short baseline acoustic system of the mother ship. Fig. 2 (c) and (d) were taken using the SeaXerocks long-range 3D seafloor imaging instrument (Thornton et al., 2016) during the KY14-01 cruise of the R/V Kaiyo in January, 2014. During the NT16-01 cruise, 12 locations around the 30 m high North Big Chimney (NBC) mound and chimney, were measured over 3 deployments. The survey area was 50$\times$50 m and the measurements were performed at 8 locations on the base part of the NBC mound (NB-1, NB-2, NB-4, NB-5, NB-7 to NB-10), 3 locations on the shoulder part of the NBC mound (NB-3, NB-6, NB-11) and 1 location

on the top of the chimney at the central part of the NBC mound (NB-12) as shown in Fig. 2 (c) and (d). The average distance between measurements was 10 m. During the KS-18-J03 cruise, 11 locations around the Bio Site, which is located by 30 m north of the NBC mound, were measured over 4 deployments. The total survey area was 25×25 m and average distance between measurements was 5 m, more densely spaced than that at the NBC mound. Since there are no public guidelines for field measurements with LIBS, we applied protocols developed based on in situ XRF surveys of minerals (L. Ge and Zhou, 2005) as a starting point for discussion on this topic. Our emphasis here is in the difference between the single and triple point measurements recommended by Ref. (L. Ge and Zhou, 2005). For terrestrial surveys, guidelines recommend triple and quintuple point measurements at 50-100 cm intervals. However, for subsea surveys, ROV repositioning is a time consuming operation and given the limited reach of the manipulator and availability of time, these measurements were replaced with single and triple measurements respectively.

- weathered or oxidised surface layer ($\sim$ 1 mm) removal using a grinder to expose a fresh surface, and
- triple point (detailed) measurements for a period of 3 $\times$ 20 minutes to obtain 3 sets of $>$ 200 well-resolved spectra with a 30 cm range interval, or
- single point (standard) measurements for a period of 20 minutes to obtain $>$ 200 well-resolved spectra.

The increased turbidity caused by rock grinding operations could potentially affect laser focusing. To mitigate this issue, sufficient time (typically a few minutes) was taken for suspended particles to settle prior to carrying out the LIBS measurements. Triple point measurements were made at 50 % of the survey locations to characterise local scale heterogeneity. Table S3 (Supplementary Material) shows a summary of measurements at the NBC mound and Bio Site where the time taken to grind the surface, LIBS measurement time, the num-

ber of analytically useful spectra for PLS calculation, the number of total laser shots fired at each point, and ratio of analytical spectra to total laser shots are shown. The method used to extract well-resolved analytical spectra is explained in section 3.1. At the NBC mound, the triple point detailed measurements were performed at 6 locations (NB-1 to NB-6) and single point measurements were performed at the rest of locations (NB-7 to NB-12). In the Bio Site, triple point detailed measurements were performed at 6 locations (BS-1 to BS-6) and single point measurements were performed at 5 locations (BS-7 to BS-11). The grinding operation took 10 minutes for a triple point measurement and 5-6 minutes for a single point measurement on average since a triple point measurement needs larger exposed surface area. The rock surface at NB-12 at the top of the chimney was not ground since the slope of the chimney is steeper than 60° and it was not possible to land stably enough to deploy the grinder. Measurements were performed for 17 minutes and 24 minutes on average at each point at the NBC mound and Bio Site, respectively, in which 2000-3000 spectra were taken, to obtain a sufficient number of well-resolved spectra. On average, 200-300 well-resolved spectra were taken at each point. The ratio of well-resolved analytical spectra was one-tenth on average because of the ROV's motion caused by surface and bottom currents, and the effects of the sea state on the mother ship causing the ROV tether cable to be pulled, which required re-positioning of the ROV and refocusing of the probe. The difference in average measurement time is attributed to the worse weather conditions during KS-18-J03, which mean that the ROV needed to be re-positioned more frequently. At some locations at the Bio Site, due to particularly severe sea conditions, the measurement required up to 40 minutes and resulted in a low ratio of analytical spectra. Rocks were collected at each location after measurements for high-accurate laboratory-based analysis. The same deposits that were measured were sampled where possible. Photos taken during measurements are shown in Fig. 4. Fig. 4 (a) shows grinding of the surface layer of the rock, (b) shows ChemiCam measurements, and (c) shows ROV sampling of the target. In Fig. 4 (b), the left and right photos were taken during a single and triple measurement at the NBC mound, respectively.

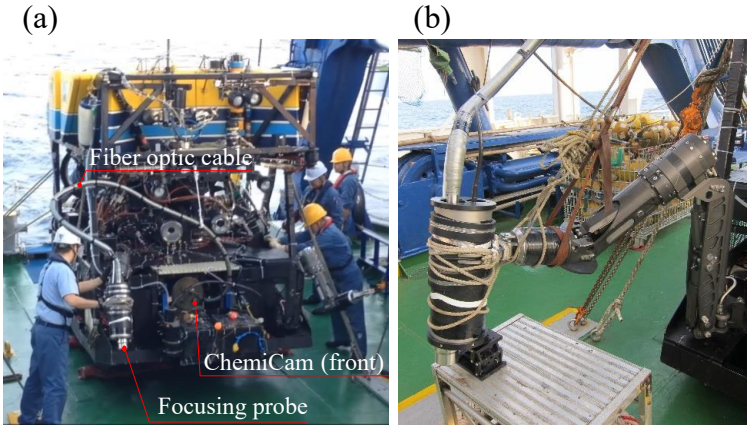

Figure 1: (a) ChemiCam mounted in the ROV Hyper-Dolphin. (b) Close up of the focusing probe and the ROV manipulator.

Grinding was performed over a large enough area to be able to visually confirm the measurement probe was placed on the ground surface. The red light seen in the right photo of Fig. 4 (b) is the light from the guide laser used to focus the probe. The main purpose of the surface grinding operation is to remove the oxidised or weathered and so potentially unrepresentative surface material in accordance with standard practice in in situ XRF monitoring. The ground depth is approximately 1 cm. However, the measurements made using LIBS is of the exposed surface and not of the bulk volume of the target, which is what is typically measured in samples and in the pelletised bulk samples that were used in the cross-validation and validation studies.

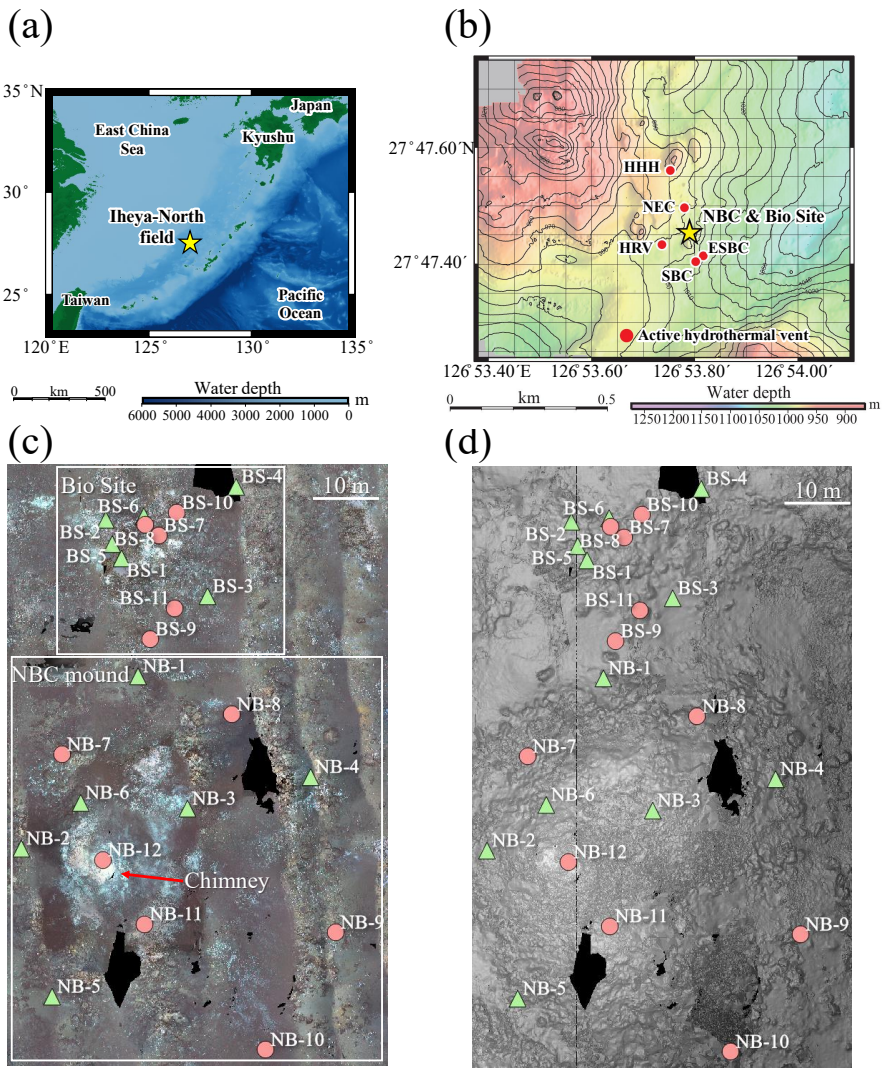

Figure 2: (a) Regional map of Iheya North field. The bathymetry in Fig. 2 was taken from the General Bathymetric Chart of the Oceans (The GEBCO_2019 Grid, 15 arc-second intervals). (b) Bathymetry of the Iheya-North hydrothermal field with locations of hydrothermal chimneys (Kawagucci et al., 2013). Depth contours are at 10 m intervals. (c) Top view projection of a 3D visual reconstruction and (d) the hillshade map generated using stereo-images (Thornton et al., 2016). The green triangles indicate locations where triple point measurements were performed (NB-1 to NB-6, and BS-1 to BS-6) and the pink circles indicate locations where single point measurements were performed (NB-7 to NB-12, and BS-7 to BS-11).

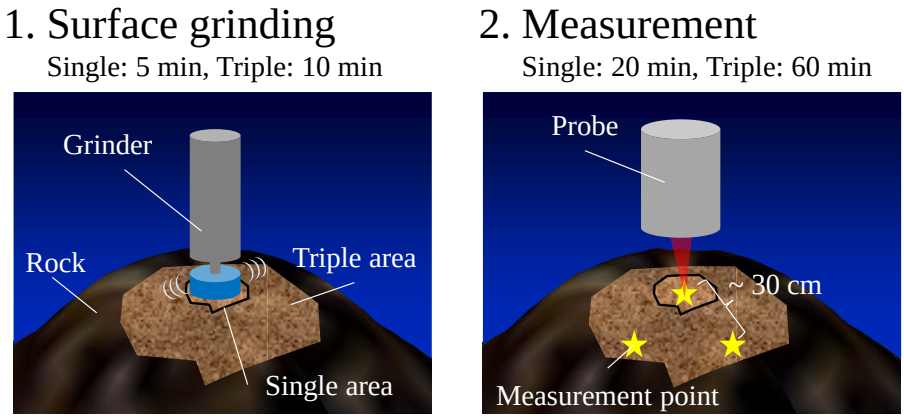

Figure 3: The in situ deep-sea LIBS measurement protocol.

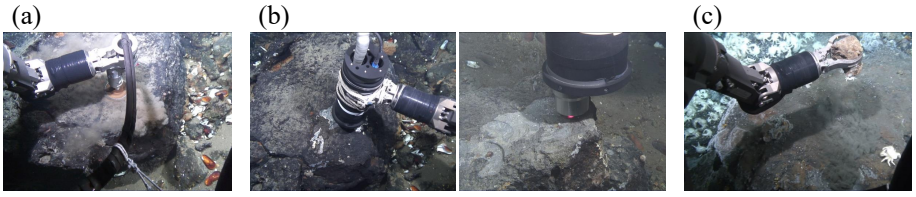

Figure 4: Dive photos of (a) Grinding, (b) measurements (left: single, and right: triple) and (c) sampling being performed during the dive surveys.

3. Methods

3.1. Signal pre-processing

Well-resolved analytical spectra were selected by setting a threshold of the Na I peak at 418.6 nm, which was seen strongly in all well-resolved spectra taken in the laboratory and on the seafloor. When targeting the surface of solids, not every laser shot results in plasma formation. Therefore, it is necessary to first identify whether the spectra observed should be analysed or discarded. For this, we use the Na I peak at 418.6 nm, which is reliably present in all well-resolved spectra taken in seawater, where the peak can be mainly attributed to the concentration of Na in seawater (ca. 2.7 %). In Ref. (Matsumoto et al., 2013), Na peaks were observed in measurements of pure Cu metal targets submerged in NaCl aqueous solutions and is a reliable indicator that a plasma has formed. Although the hydrothermal deposits targeted in this work are known to contain some Na, the concentration in the sulphide-rich and sulphate-rich chimneys is less than 1 % (Nozaki et al., 2016). Moreover, the origin of the peak itself does not have an impact on subsequent data processing since the concentration of Na is not included in quantitative analysis. Although it is possible to generate a plasma in bulk liquids directly with no solid surface to focus the laser on, this requires a minimum of 15 mJ long pulse using the focusing optics on ChemiCam (Thornton et al., 2014, 2015). The pulse energy used in this work was 5 mJ, which can only generate plasma on a solid target. Since quantification was limited to Cu, Pb, and Zn and the concentrations of these elements in seawater and even in pristine hydrothermal fluids are less than 200 μM (Kawagucci et al., 2013), the effect of contribution from the seawater and hydrothermal fluid on quantification results is negligible. Selected signals were pre-processed as follows; 1) normalisation, 2) smoothing, and 3) background subtraction (Andrade-Garda et al., 2013). Signals were normalised by the total intensity of the whole spectrum. For noise reduction of signals, a three points weighted average smoothing method was used (Andrade-Garda et al., 2013). The background continuum was subtracted using a polynominal function (Gor-

nushkin et al., 2003, Jurado-Lopez and de Castro, 2002). Each spectrum is divided into 2 parts and the background was modelled and subtracted using an eighth-order function for the shorter wavelength range and sixth-order function for the longer wavelength range, which were experimentally determined. Fig. 5 shows examples of spectra taken in the laboratory of samples submerged in water at atmospheric pressure, and spectra taken in situ at depths of $\sim 1000\,\mathrm{m}$ during the survey. The in situ spectra are from NB-3, NB-4, NB-11 and NB-12, and the laboratory measurements are of rock samples recovered from these locations. Elements corresponding to the emission lines of interest were identified based on Ref. (Kramida et al., 2012). The peak identification here is only for illustrative purposes since the method described in this work does not require peaks to be manually identified. No obvious self-absorbed peaks of Cu, Pb and Zn were observed. Fe, Cu, Pb, and Zn peaks are seen in all spectra with a prominent Na peak at 418.6 nm. Although the Na peak was observed more strongly in most of the spectra taken in situ, other peaks did not show any obvious differences. This does not impact subsequent analysis since the Na peak is removed from the spectral range for analysis since it is not certain what proportion of contribution is from the rocks and from seawater.

3.2. Partial least squares regression model

The PLS1 algorithm was used to model each element's concentration. This allows for simple interpretation of each component's loading response (Haaland and Thomas, 1988). Each model was constructed by taking the average of spectra taken under the same conditions, and multiple data sets were generated for each condition. A boot-strap method was used to increase the number of datasets by random sampling (Efron, 1979). 30 sets of 70 averaged spectra were used as this was found to be suitable based on XRF analysis of sample heterogeneity, as described in section 3.3. It should be noted that 70 analytical spectra were not achieved at some triple point measurement locations during the LIBS measurements, *e.g.* BS-2, BS-4, and BS-6. These points were removed from the in situ data evaluation and the data at these locations were evaluated

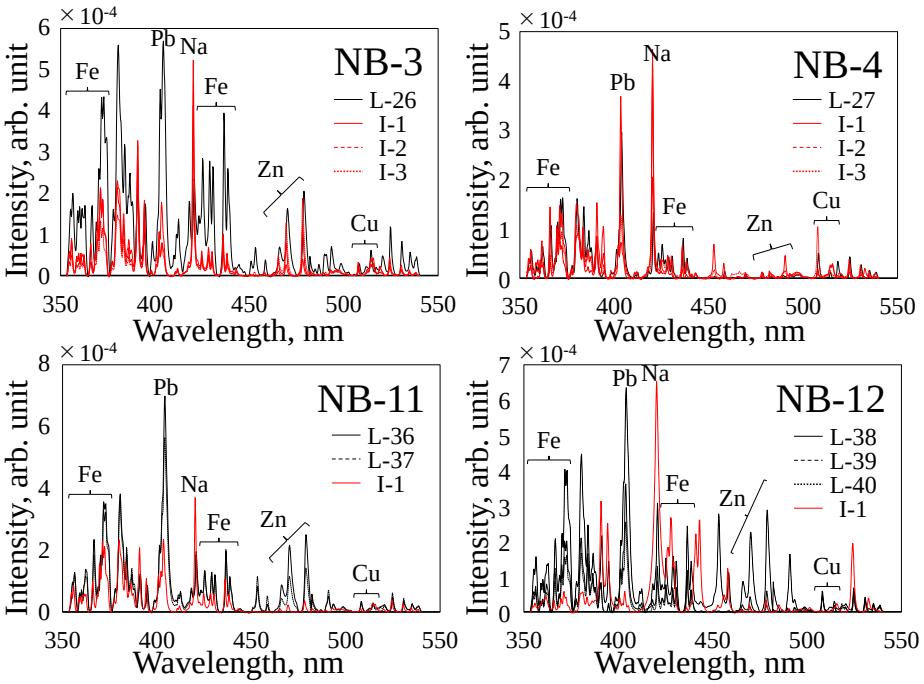

Figure 5: Examples of spectra taken in laboratory and at the hydrothermal deposit (NB-3, NB-4, NB-11, NB-12). The black and red lines indicate spectra taken in laboratory and at the hydrothermal deposit, respectively. The name of the elements which the emission lines stem from are written above the corresponding peaks. "L-" and "I-" in the legend indicate spectra taken in laboratory and in situ, respectively. The number with "L-" is the sample identification number. The spectra taken at NB-3 and NB-4 where triple point measurements were performed were superimposed as I-1, 2, and 3.

using the remaining points that had sufficient valid spectra. The PLS models were constructed using 32 samples (1 to 23, 25 to 27, 32, 33, 35, and 38 to 40), and their accuracy was characterised using a standard leave-one-out cross-validation (LOOCV), where measurements of 1 sample were used to test and verify the models constructed using measurements of the remaining samples. The optimal numbers of LVs for the PLS model were chosen to give the lowest root mean square error of cross-validation (RMSECV) with a contribution rate of more than 95 %. Since the output is the elemental concentration, values determined to be negative were set to zero. 8 samples (24, 28 to 31, 34, 36, 37), which were not used to train any of the regression models, were used for validation to verify the cross-validation accuracy. The in situ data were analysed using the cross-validation model. The accuracy of the regression model was evaluated by the absolute errors (AEs) and REs given as:

$$AE = |\hat{y} - y| \tag{1}$$

$$RE = \frac{|\hat{y} - y|}{\hat{y}} \times 100 \tag{2}$$

where y and $\hat{y}$ represent the predicted and reference concentration, respectively.

3.3. Sample inhomogeneity

The spectra were averaged to reduce the effect of target inhomogeneity, and multiple data sets were analysed to characterise the consistency of the results. In order to determine appropriate averaging and set numbers, elemental-wise spatial distributions of sample surfaces were analysed for 8 samples using a high-resolution XRF scanner (Hitachi High-Technologies Ltd., EA6000VX). The XRF measurement spot size was 30 μm and measurement time per spot was 10 ms. It is noted that the XRF scanner used does not give quantitative concentration, so the relative intensity is used as a criteria to assess the inhomogeneity of each element. Fig. 6 shows an example of the distribution of Cu, Pb, and Zn on the surface of sample 16, where the top images show the distributions of the surface of a bulk pellet, as is measured using LIBS in the laboratory experiment, and the bottom for an original rock surface, similar to the conditions expected

during in situ measurements. Inhomogeneity was analysed for both pellets and rock surfaces. Several spots with the strong intensities are clearly seen in the images of all elements both for the pellet and the corresponding rock samples, where in general inhomogeneity is more pronounced for the rock surfaces than the pellet. The laser spot size of the LIBS measurements is 120 μm in this study. The area sampled by each shot is not sufficient to describe the spatial inhomogeneity observed, and so multiple measurements need to be made. To analyse the distribution quantitatively, measurements with a 120 μm foot-print were simulated within a 5×5 mm box (indicated in the figures). Pixels for averaging were randomly chosen by the boot-strap method, and the intensities were averaged. The process was repeated multiple times. Fig. 7 shows the standard deviations of the intensities of different averaging numbers (left) and different set numbers (right) for (a) Cu, (b) Pb, and (c) Zn for pellet samples. 8 different samples with non-zero element concentrations were analysed. The standard deviations decrease steeply up to 40 averaged measurements and are stable after 70 averaged measurements for all samples and elements. The standard deviations of the intensity of XRF analysis of rocks and pellets are compared in Fig. 8. The standard deviations of rocks are approximately 2 times larger than pellets for a 5×5 mm spatial scale, converging after 70 samples. After convergence, the average value extracted remains within 10 % standard deviation. This is considered acceptable for the purposes of this study to characterise inhomogeneity of a single point over these spatial scales. Regarding the set number, there is no obvious trend for pellet and rock samples as seen in Figs. 7 and 8. The set number was set to 30 to avoid fluctuations with smaller set numbers seen in some samples.

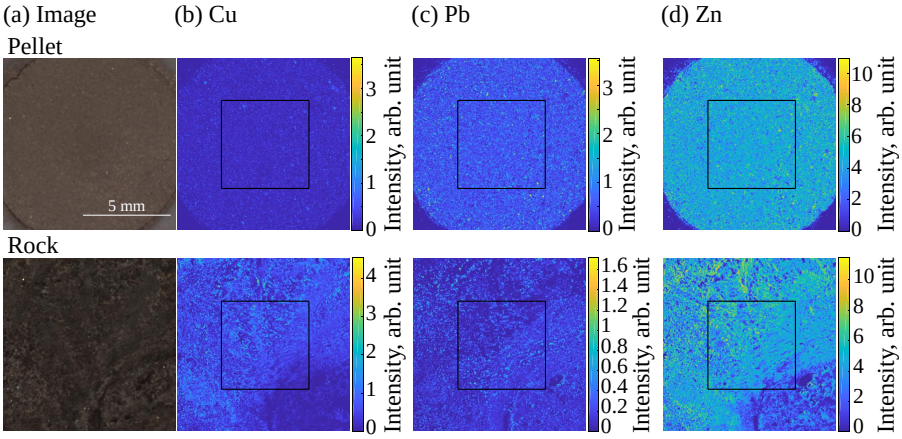

Figure 6: (a) The surface image and distributions of (b) Cu, (c) Pb, and (d) Zn of sample 16. The top images were taken for a bulk pellet, whereas the bottom ones were taken for a rock piece. The 5 × 5 mm black boxes in (b) to (d) indicate the area used to analyse surface inhomogeneity.

4. Results and discussions

4.1. Cross-validation and validation results

4.1.1. Cross-validation results

The PLS calibration models constructed are shown in Fig. 9 where the plot shows a linear model of the calculated concentration as a function of the benchmark concentration (indicated as actual concentration) and 95 % confidence intervals. The optimal numbers of LVs to minimise RMSECV were 13 for Cu, 11 for Pb and 6 for Zn. The circles indicate the average results calculated from the 30 sets of averaged measurement for each sample with the standard deviations for cross-validation (black) and validation (red), respectively. The black and red outline marks indicate the values calculated negative and set to 0 for cross-validation and validation, respectively. The black solid and dotted lines indicate the linear regression and $y = x$, respectively. The grey zones in the figures represent the 95 % confidence intervals of the regression analysis. All slopes of the linear regression lines are smaller than 1, which are often seen in

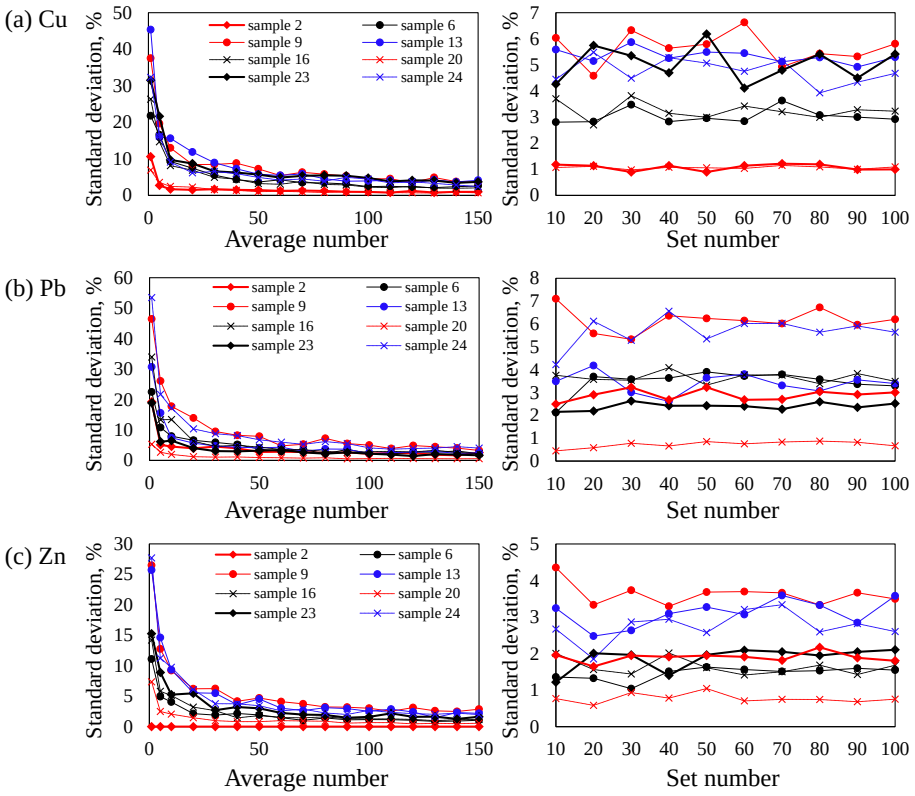

Figure 7: Standard deviations of the intensity of XRF analysis of pellets for (a) Cu, (b) Pb, and (c) Zn. The x-axes of the figures on the left-hand side are the averaging number where the dataset number was fixed at 30, and the x-axes of the figure on the right-hand side are the number of averaging sets where the averaging number was fixed at 70.

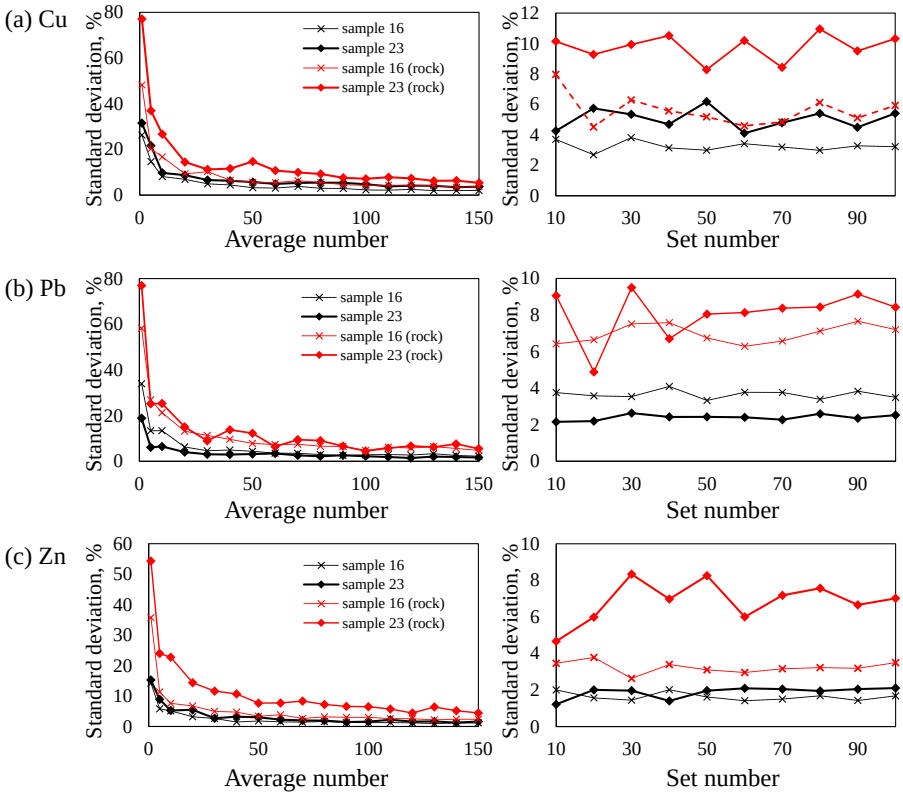

Figure 8: Standard deviations of the intensity of XRF analysis of (a) Cu, (b) Pb, and (c) Zn for comparison of pellets and rocks. The x-axes of the figures on the left-hand side are the averaging number where the dataset number was fixed at 30, and the x-axes of the figure on the right-hand side are the number of averaging sets where the averaging number was fixed at 70. The black and red lines indicate bulk pellets and rock surfaces of the same samples, respectively.

PLS calculations using LIBS data (Clegg et al., 2009, Martin et al., 2013), and is also expected due to setting a 0 % lower limit for the predicted output. Pb has the closest linear regression to $y = x$ and the highest R^2 value of 0.75. Zn has an R^2 value of 0.68, and Cu has an R^2 value of 0.58. The values of AEs and REs are summarised in Table 1. To compare results from 3 elements with the different concentration ranges, "Band" 1 to 5 indicate normalised bands of actual concentration of 0 to 0.2, 0.2 to 0.4, 0.4 to 0.6, 0.6 to 0.8, and 0.8 to 1 where the minimum and maximum concentration of sample sets for each element are set as 0 and 1, respectively. The ranges of actual concentrations according to the range band are described as "Range". "Num." indicates the number of samples in each range band. The AEs are ~ 1 % for Cu, 2 to 5 % for Pb, and 6 to 11 % for Zn in all ranges, which indicates that AEs are independent of the bands. The difference between the AEs of elements might come from the concentration range of the models since the maximum concentration of Cu in the model is 8.02 % whereas that of Pb and Zn are larger, at 26.5 and 51.2 %, respectively. As a result, the REs in the low concentration range are large, and beyond reliable quantification of compositions in the lowest concentration band. REs of higher concentration ranges, *i.e.* the bands 2 to 5, have stable values around 20 %, except for the band 2 of Zn, which is 53 %. For these concentration ranges, the accuracy of the PLS calculation has an average RE of 25.7 %. From the results, the reliable range of PLS calculations in this study is determined as the bands 2 to 5, which is equivalent to 0.2 to 1 of the modelled concentration range for each element.

4.1.2. Validation results

The AEs and REs calculated from the results of 8 independent validation samples not used to train any of the regression models are summarised in Table 2. The validation results follow the trends seen in the cross-validation. While AEs and REs of validation in the band 1 is around 70 %, which is less than the values of cross-validation, it is still considered too high for reliable analysis. In the bands 2 to 5, the average RE is 24.3 %, which is in close agreement to

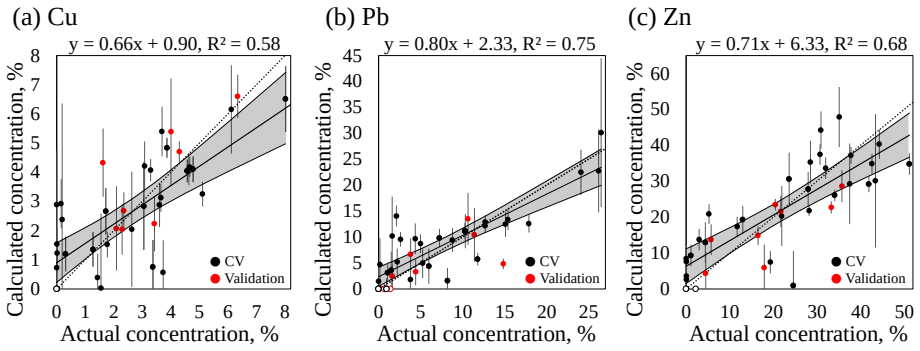

Figure 9: PLS results of (a) Cu, (b) Pb, and (c) Zn. The black and red circle indicate the average results calculated from the 30 sets of averaged measurement for each sample with the standard deviations for cross-validation and validation, respectively.

Table 1: AEs and REs of the PLS calculations for Cu, Pb, and Zn during cross-validation. "Band" 1 to 5 indicate the bands of actual concentration of 0 to 0.2, 0.2 to 0.4, 0.4 to 0.6, 0.6 to 0.8, and 0.8 to 1 where the minimum and maximum concentration of sample sets for each element are set as 0 and 1, respectively. The ranges of actual concentrations according to the range band are described as "Range". "Num." indicates the number of samples in each range band.

	Cu				Pb				Zn			
Band	Range (%)	Num.	Ave. AE (%)	Ave. RE (%)	Range (%)	Num.	Ave. AE (%)	Ave. RE (%)	Range (%)	Num.	Ave. AE (%)	Ave. RE (%)
1	0 to 1.60	13	1.14	9830	0 to 5.30	17	3.10	>10000	0 to 10.2	11	6.13	>10000
2	1.60 to 3.21	5	0.62	30.8	5.30 to 10.6	6	2.18	27.7	10.2 to 20.5	3	7.94	52.8
3	3.21 to 4.81	11	1.15	27.0	10.6 to 15.9	5	2.29	17.6	20.5 to 30.7	7	7.48	28.9
4	4.81 to 6.42	2	0.95	18.5	15.9 to 21.2	1	5.32	29.7	30.7 to 41.0	6	7.42	21.9
5	6.42 to 8.02	1	1.51	18.9	21.2 to 26.5	3	2.90	11.2	41.0 to 51.2	5	10.84	24.1

Table 2: AEs and REs from the validation of Cu, Pb, and Zn.

Band	Cu				Pb				Zn			
	Range (%)	Num.	Ave. AE (%)	Ave. RE (%)	Range (%)	Num.	Ave. AE (%)	Ave. RE (%)	Range (%)	Num.	Ave. AE (%)	Ave. RE (%)
1	0 to 1.60	0	-	-	0 to 5.30	5	1.38	70.7	0 to 10.2	2	4.08	71.8
2	1.60 to 3.21	4	0.83	48.2	5.30 to 10.6	0	-	-	10.2 to 20.5	2	5.57	30.7
3	3.21 to 4.81	2	0.99	26.2	10.6 to 15.9	3	4.62	34.3	20.5 to 30.7	1	0.15	0.71
4	4.81 to 6.42	1	0.26	4.02	15.9 to 21.2	0	-	-	30.7 to 41.0	2	8.86	25.9
5	6.42 to 8.02	0	-	-	21.2 to 26.5	0	-	-	41.0 to 51.2	0	-	-

the results of the cross-validation study. To remove signals of samples with low concentrations of targeted elements from the validation data, a cut-off limit of the height of peaks of targeted elements can be set. Alternatively, to improve the accuracy of the PLS model for the low concentration range, a method which can first determine an optimal range of a PLS model, such as the sub-model method suggested in the ref. (Anderson et al., 2017), could potentially be applied in future studies.

4.2. Results of in situ data

4.2.1. Comparison of pellets and rocks

The PLS results of in situ data taken at the NBC mound and the Bio Site are shown in Table 3. In situ data consists of measurements of the ground surface of natural hydrothermal rock deposits taken at a water depth of 1000 m as described in section 2.2.2. Since reliable results are not expected from band 1, concentrations of band 1 were removed from analysis. Compared to the cross-validation and validation results of bulk pellets shown in Tables 1 and 2, REs are large with respect to the benchmark values, with an average of 54 %. This is approximately double the average RE for the pellets, which is in agreement with the trends seen in the XRF measurements in Fig. 8. While the results are in agreement, there are however, some differences in concentrations observed between both the individual measurement sets constituting a triple point measurement, and samples that were collected from the same location

Table 3: AEs and REs from the in situ data of Cu, Pb, and Zn taken at the NBC mound and the Bio Site.

Band	Cu				Pb				Zn			
	Range (%)	Num.	Ave. AE (%)	Ave. RE (%)	Range (%)	Num.	Ave. AE (%)	Ave. RE (%)	Range (%)	Num.	Ave. AE (%)	Ave. RE (%)
2	1.60 to 3.21	4	0.80	42.6	5.30 to 10.6	7	4.20	54.6	10.2 to 20.5	3	17.1	98.1
3	3.21 to 4.81	2	1.66	46.2	10.6 to 15.9	1	0.97	8.22	20.5 to 30.7	4	8.77	38.6
4	4.81 to 6.42	1	4.93	77.7	15.9 to 21.2	0	-	-	30.7 to 41.0	3	16.2	42.9
5	6.42 to 8.02	1	6.34	79.1	21.2 to 26.5	0	-	-	41.0 to 51.2	0	-	-

that are not described by the laboratory analysis. The two possibilities are lateral surface inhomogeneity on scales > 5 mm that were characterised in Fig. 8 where another possibility is because the concentration of elements can vary significantly within inner and outer cross-sectioned profile of the targets. Ref. (Halbach et al., 1989) reported that a 2 cm depth difference from the surface layer of a hydrothermal deposit from the Okinawa Trough shows 10 times higher concentration of Zn than at the surface. In ref. (Noguchi et al., 2011), variations of main elements within a 90 cm long chimney taken in the Okinawa Trough were described as 0.01 to 4 % for Cu and 0 to 20 % for Zn. While rocks measured using LIBS were targeted for sampling during the ROV dive surveys, some were not exact ones measured but were sampled within arms reach due to limitations of the ROV's ability to sample the desired target. This could cause unmatched quantitative results between samples that had their bulk composition analysis, and rock surfaces that represent a specific depth layer. The next subsection looks at the effect of large-scale inhomogeneity to quantitative results by comparing the results of triple and single point measurements and samples recovered from adjacent locations in more detail.

4.2.2. Comparison of triple and single points

To investigate whether the results of triple point measurements represent larger-scale inhomogeneity within the spatial interval (~ 30 cm) between measurements, or if the variation observed is just a function of the number of mea-

surements being larger is effective, the results of triple point measurements and single point measurements where the large number (> 210) of spectra were obtained from one location are compared in Fig. 10. Locations at the NBC mound and the Bio Site where the element concentration range is in bands 2 to 5 are shown. The grey and black bars indicate the actual concentrations and calculated concentration from triple point measurements (values from 3 independent points are shown as 1, 2, and 3), respectively. The pink and red bars indicate the actual concentrations and calculated concentrations from single point measurements (3 independent results with different 30 datasets calculated from 70 averaged spectra are shown for each measurement as a, b, and c), respectively. Actual concentrations of all rocks taken at each location where multiple rocks were obtained are shown independently. The numbers in the second row indicate the sample identification numbers shown in Table S1 (Supplementary Material). The grey background shows the average concentration of 3 points for triple point measurements, and the pink background shows the average concentration of 3 datasets for single point measurements. It is clear that the actual concentrations of rocks taken at the same locations have large variance, and the concentrations for triple point measurements vary between local locations intervals ($\sim 30\,\mathrm{cm}$), whereas similar concentrations were calculated from 3 different datasets for the single point measurements. It can be said from the results that large-scale inhomogeneity does exist and multiple measurements are needed for express this. Differences between the results of in situ measurements and sample benchmark values can be caused by the this effect. Since the ablation mass of the analyte in LIBS measurements is of the order of ng per shot compared to several tens of mg order of bulk powder for ICP-MS, it can be said that LIBS is more sensitive than traditional methods of laboratory analysis to the effects of local-scale target inhomogeneity. While this can be useful for high-resolution rock surface analysis, obtaining representative composition that is comparable to traditional sampling at a specific measurement location requires measurement of the bulk material, and varying location of the measurement over a multitude of scales to gather more representative information. Since LIBS measurements

are semi-destructive, ablating a small amount of material with each shot, one way to further increase bulk information is to increase the number of analytical spectra. This can be achieved by increasing the frequency of laser shots, which is realistic considering commercial lasers that routinely fire pulsed at $>$ 30 Hz pulse repetition rates. Another solution is to make in situ measurement of slurry during the grinding process of rocks. It has been shown that analytically useful LIBS spectra can be obtained from an ore slurry in the laboratory using the same laser and detector system as this work (Nakajima et al., 2019). This could realise bulk measurement during the grinding process efficiently and lead to further improvement in the estimates of mineral distributions.

4.2.3. Grinding effect

During in situ measurements, NB-12 was the only location where the grinding process was skipped due to the steep slope making landing impossible. Considering the quantification results of NB-12 in Fig. 10, while the concentration of Cu is calculated close to the actual concentration, Pb and Zn have poor AEs compared to other in situ data regarding these elements. This might be because of lack of the grinding process and leaching of surface layer composition over extended periods, or enrichment effects during deposition.

4.2.4. In situ chemical map

Figure 11 shows the map of the survey area with the information of Cu, Pb, and Zn concentrations calculated from (a) the in situ data and (b) benchmark values obtained from ICP-MS. The size of the circle indicates the difference of the bands 2 to 5 and the reliable accuracy range is limited to samples with concentrations in this range. Visualisation of the in situ concentration shows similar trends in element distribution to the benchmark values. As discussed in section 4.1.1 and 4.1.2, the average RE of quantitative results was obtained as 25 %. While it is one order of magnitude higher than typical values taken for Cu, Pb and Zn in rocks using LIBS and XRF in air and needs to be reduced in future studies, the advantage of in situ analysis using LIBS is that the number

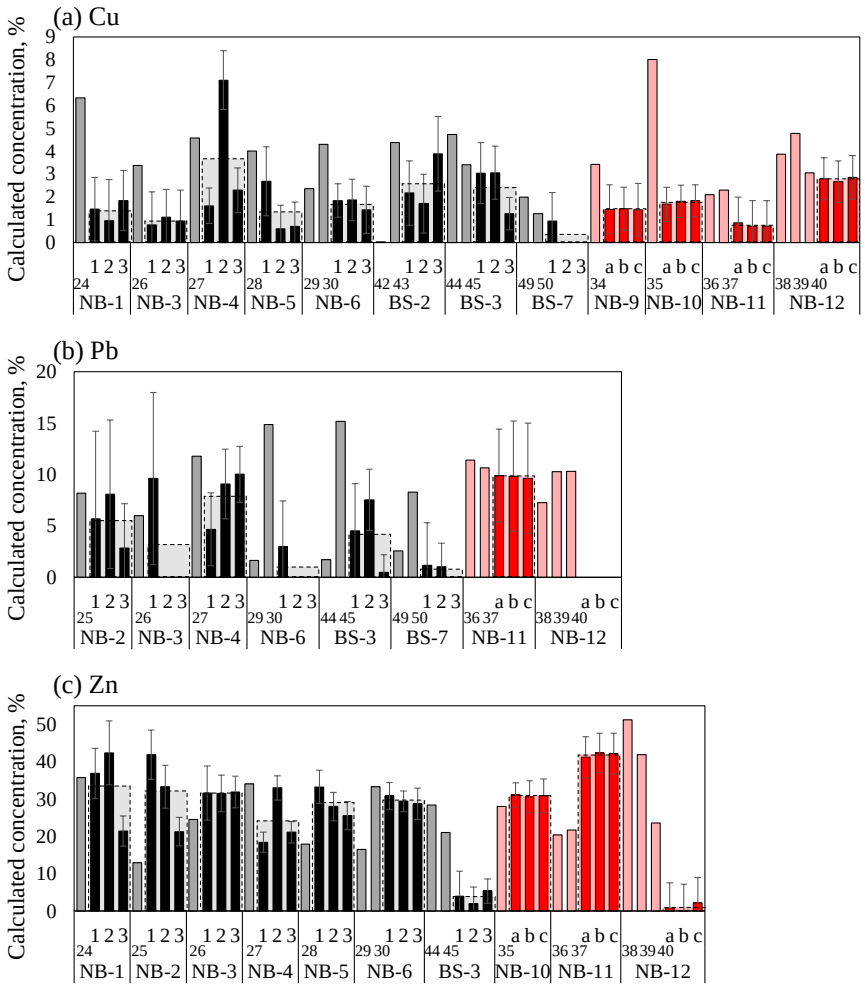

Figure 10: Comparison of quantitative results obtained from triple and single point measurements. The grey and black bars indicate the actual and calculated concentration from triple point measurement (the value from each point is shown as 1, 2, and 3), respectively. The pink and red bars indicate the actual and calculated concentration from single point measurement (3 independent results with different 30 datasets calculated from 70 averaged spectra are shown for each measurement shown as a, b, and c), respectively. The numbers in the second row indicate the sample identification numbers. The grey and pink backgrounds show the average concentration of 3 points for triple point measurements and the average concentration of 3 datasets for single point measurements, respectively.

of measurement points can be increased significantly compared to analysis of sampled rocks. For rocks and deposits, the sampling capacity of submersibles is limited by available space for storage and upthrust available for recovery. Once either of these limits is reached, it is necessary to recover the samples before continuing survey operations. This is particularly limiting for platforms with otherwise long mission duration, *e.g.* field resident ROVs (Purser et al., 2013, Doya et al., 2017) where there are few opportunities to transit through the water column, and for platforms with limited upthrust, such as AUVs which rely on drop weights or buoyancy engines (typically no more than a few kilograms capacity) (Thornton, 2019), or hybrid ROVs that have near neutral buoyancy and use thin fibre-optic umbilical cables that cannot be used to lift the increased weight of platform. Although in some operations, purpose-designed lift systems can be loaded by submersibles to recover samples independently of the platform, this introduces operational complexity (Miller et al., 2018). In situations like these, in situ measurement can potentially increase the resolution and efficiency of chemical surveys. In addition to situations where the platform's sampling capacity is a limited factor, there are also applications where real-time knowledge of mineral distribution for multi elements is of value. For applications such as mining, it is valuable to know the composition of the target in situ to inform real-time decisions about whether to continue drilling and sample recovery operations and so avoid an unnecessary effort of low-grade substrate recovery (Nakajima et al., 2019). For applications such as pollution monitoring, knowledge of the target composition and concentration of elements can derisk or mitigate the need for handling of toxic substances (Saeki et al., 2014). Another interesting development is applications investigating extraterrestrial oceans, with several groups investigating chemical and biological survey of under-ice oceans of Titan, Encaledus and Europa where a sample return would be significantly increase operational cost and complexity (Fortes, 2000, Hsu et al., 2015, Lowell and DuBose, 2005, Sobron et al., 2018).

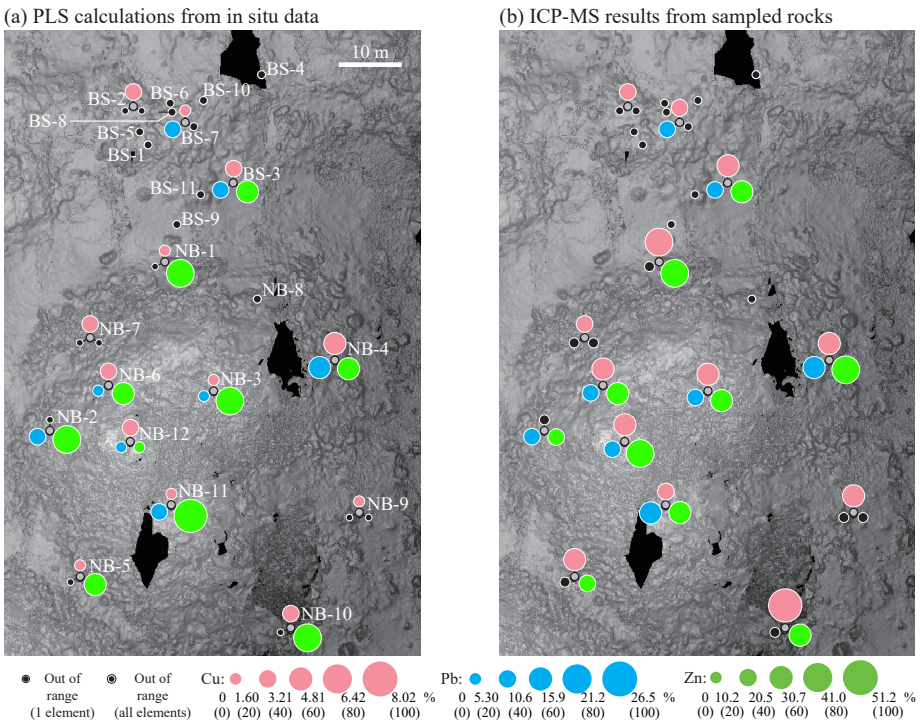

Figure 11: Chemical map of Cu, Pb, and Zn created from (a) the PLS analysis of in situ data and (b) benchmark values concentrations for comparison. Points where rocks with benchmark concentrations over 0.2 of the concentration ranges of the cross-validation models are shown.

5. Conclusions

- This work has demonstrated for the first time in situ quantification of Cu, Pb, and Zn in deep-sea minerals at $> 1000\,\mathrm{m}$ water depth by combining LIBS and multivariate analysis and generated maps of elemental distribution in a deep-sea hydrothermal vent system that are in broad agreement with distribution patterns of sampling based benchmark values.

- The reliable range of concentrations determined by cross-validation studies and independent validation is between 0.2 and 1 of the range of concentrations used to train the PLS models.

- An average RE of $25\,\%$ was achieved in this range for all 3 elements that were quantified for powder submerged bulk pellets.

- The effects of target mineral inhomogeneity can be addressed by increasing the number of shots, where for a $120\,\mu\mathrm{m}$ laser footprint, for hydrothermal pellets and natural rock surfaces, averaging 70 repetitions was sufficient for convergence in the setup in this study, where natural rock surfaces exhibited a larger level of stable variation after convergence.

- Measurements of rock surfaces are more susceptible to the effects of inhomogeneous element distribution, with both XRF and LIBS measurements showing approximately double the variation compared to ground pellets for the hydrothermal samples used in this work.

- The representation of bulk mineral composition can be improved for a given number of in situ measurements by locally moving the measurement location over small distance intervals of $\sim 30\,\mathrm{cm}$.

- The technique enables a significant increase of measurement points to obtain detailed mineral distributions, real-time chemical feedback during deep-sea operations and chemical surveys in situations or with platforms where sample recovery is not possible.

6. Future recommendation

- Developments of increase long pulse laser repetition rates should be prioritised to increase accuracy and speed of in situ surveys.
- Optical setups to measure ore slurry in situ should be prioritised for representative bulk measurement and application to real-time mineral sorting during mining.

Acknowledgement

The project is funded by the Japanese Ministry of Education, Culture, Sports, Science and Technology under the Program for the development of fundamental tools for the utilization of marine resources. We gratefully acknowledge the support from members of the steering panel; T. Takeuchi, T. Fujii, K. Iizasa, the late K. Tamaki, T. Ura, H. Sugimatsu, T. Yamamoto, K. Okino and J. Ishibashi. The study was supported in part by the JSPS Grand-in-Aid for JSPS Fellows (No.268488). The authors thank the Hyper-Dolphin 3000 team and R/V Natsushima and R/V Shinseimaru crew for their assistance during the NT16-01 and KS-18-J03 cruises. We thank A. Matsumoto, M. Yelameli and S. Miyagawa for their support collecting and analysing samples and their help during experiments with ChemiCam, and T. Sato and K. Yasukawa for discussions and advice for analytical methods. The cross-validation and validation dataset, composition data for all measured elements, and raw spectra with calibration data are released with this publication for future benchmark studies: https://github.com/ocean-perception/chemicam_open_database.

R. B. Anderson, S. M. Clegg, J. Frydenvang, R. C. Wiens, S. McLennan, R. V. Morris, B. Ehlmann, and M. Darby Dyar. Improved accuracy in quantitative laser-induced breakdown spectroscopy using sub-models. *Spectrochimica Acta Part B: Atomic Spectroscopy*, 29:49–57, 2017.

J. M. Andrade-Garda, A. Carlosena-Zubieta, R. Boque-Marti, and J. Ferre-Baldrich. Partial least-squares regression. In J. M. Andrade-Garda, editor,

Basic chemometric techniques in atomic spectroscopy, pages 280–347. The Royal Society of Chemistry, Cambridge, 2013.

A. Bodenmann, B. Thornton, and T. Ura. Development of long range color imaging for wide area 3D reconstruction of the seafloor. In *Proceedings of 2013 IEEE International Underwater Technology Symposium (UT)*, Tokyo, Japan, 2013. URL `https://ieeexplore.ieee.org/abstract/document/6519824`.

A. Bodenmann, B. Thornton, R. Nakajima, and T. Ura. Methods for quantitative studies of seafloor hydrothermal systems using 3D visual reconstructions. *Robomech Journal*, 4:22, 2017a.

A. Bodenmann, B. Thornton, and T. Ura. Generation of high-resolution three-dimensional reconstructions of the seafloor in color using a single camera and structured light. *Journal of Field Robotics*, 34:833–851, 2017b.

T. F. Boucher, M. V. Ozanne, M. L. Carmosino, M. D. Dyar, S. Mahadevan, E. A. Breves, K. H. Lepore, and S. M. Clegg. A study of machine learning regression methods for major elemental analysis of rocks using laser-induced breakdown spectroscopy. *Spectrochimica Acta Part B: Atomic Spectroscopy*, 107:1–10, 2015.

A. Ciucci, M. Corsi, V. Palleschi, S. Rastelli, A. Salvetti, and E. Tognoni. New Procedure for Quantitative Elemental Analysis by Laser-Induced Plasma Spectroscopy. *Applied Spectroscopy*, 53:960–964, 1999.

S. M. Clegg, E. Sklute, M. D. Dyar, J. E. Barefield, and R. C. Wiens. Multivariate analysis of remote laser-induced breakdown spectroscopy spectra using partial least squares, principal component analysis, and related techniques. *Spectrochimica Acta Part B: Atomic Spectroscopy*, 64:79–88, 2009.

D. Death, A. Cunningham, and L. Pollard. Multi-element analysis of iron ore pellets by Laser-induced Breakdown Spectroscopy and Principal Components Regression. *Spectrochimica Acta Part B: Atomic Spectroscopy*, 63:763–769, 2008.

721 D. Death, A. Cunningham, and L. Pollard. Multi-element and mineralogical
722 analysis of mineral ores using laser induced breakdown spectroscopy and
723 chemometric analysis. *Spectrochimica Acta Part B: Atomic Spectroscopy*, 64:
724 1048–1058, 2009.

725 C. Doya, D. Chatzievangelou, N. Bahamon, A. Purser, F. C. De Leo, S. K. Ju-
726 niper, L. Thomsen, and J. Aguzzi. Seasonal monitoring of deep-sea megaben-
727 thos in Barkley Canyon cold seep by internet operated vehicle (IOV). *PLoS*
728 *ONE*, 12:1–20, 2017.

729 B. Efron. Bootstrap methods: another look at the jackknife. *The Annals of*
730 *Statistics*, 7:1–26, 1979.

731 A. D. Fortes. Exobiological Implications of a Possible Ammonia-Water Ocean
732 inside Titan. *Icarus*, 146:444–452, 2000.

733 A. D. Giacomo, M. Dell′Aglio, F. Colao, and R. Fantoni. Double pulse laser
734 produced plasma on metallic target in seawater: basic aspects and analytical
735 approach. *Spectrochimica Acta Part B: Atomic Spectroscopy*, 59:1431–1438,
736 2004.

737 A. D. Giacomo, A. D. Bonis, M. Dell′Aglio, O. De Pascale, R. Gaudiuso, S. Or-
738 lando, A. Santagata, G. S. Senesi, F. Taccogna, and R. Teghil. Laser Ablation
739 of Graphite in Water in a Range of Pressure from 1 to 146 atm Using Single
740 and Double Pulse Techniques for the Production of Carbon Nanostructures.
741 *The Journal of Physical Chemistry C*, 115:5123–5130, 2011.

742 I. B. Gornushkin, P. E. Eagan, A. B. Novikov, B. W. Smith, and J. D. Wineford-
743 ner. Automatic correction of continuum background in laser-induced break-
744 down and Raman spectrometry. *Applied Spectroscopy*, 57:197–207, 2003.

745 J. Guo, Y. Lu, K. Cheng, J. Song, W. Ye, N. Li, and R. Zheng. Development of
746 a compact underwater laser-induced breakdown spectroscopy (LIBS) system
747 and preliminary results in sea trials. *Applied Optics*, 56:8196–8200, 2017.

748 D. M. Haaland and E. V. Thomas. Partial least-squares methods for spec-
749 tral analyses. 1. Relation to other quantitative calibration methods and the
750 extraction of qualitative information. *Analytical Chemistry*, 60:1193–1202,
751 1988.

752 P. Halbach, K. Nakamura, M. Wahsner, J. Lange, H. Sakai, L. Käselitz, R.-
753 D. Hansen, M. Yamano, J. Post, B. Prause, and S. R. Probable modern
754 analogue of Kuroko-type massive sulphide deposits in the Okinawa Trough
755 back-arc basin. *Nature*, 338:496–499, 1989.

756 K. K. Herrera, E. Tognoni, N. Omenetto, B. W. Smith, and J. D. Wine-
757 fordner. Semi-quantitative analysis of metal alloys, brass and soil samples
758 by calibration-free laser-induced breakdown spectroscopy: recent results and
759 considerations. *Journal of Analytical Atomic Spectrometry*, 24:413–425, 2009.

760 H. Hou, Y. Li, Y. Tian, Z. Yu, and R. Zheng. Plasma condensation effect in-
761 duced by ambient pressure in laser-induced breakdown spectroscopy. *Applied*
762 *Physics Express*, 7:032402, 2014.

763 H. W. Hsu, F. Postberg, Y. Sekine, T. Shibuya, S. Kempf, M. Horányi,
764 A. Juhász, N. Altobelli, K. Suzuki, Y. Masaki, T. Kuwatani, S. Tachibana,
765 S. I. Sirono, G. Moragas-Klostermeyer, and R. Srama. Ongoing hydrothermal
766 activities within Enceladus. *Nature*, 519:207–210, 2015.

767 A. Jurado-Lopez and M. D. L. de Castro. Laser-induced breakdown spectrome-
768 try in the jewellery industry. Part I. Determination of the layer thickness and
769 composition of gold-plated pieces. *Journal of Analytical Atomic Spectrometry*,
770 17:544–547, 2002.

771 S. Kawagucci, J. Miyazaki, R. Nakajima, T. Nozaki, Y. Takaya, Y. Kato,
772 T. Shibuya, U. Konno, Y. Nakaguchi, K. Hatada, et al. Post-drilling changes
773 in fluid discharge pattern, mineral deposition, and fluid chemistry in the iheya
774 north hydrothermal field, okinawa trough. *Geochemistry, Geophysics, Geosys-*
775 *tems*, 14:4774–4790, 2013.

776 Y. L. L. Ge, W. Lai and S. Zhou. In situ applications of fpXRF tech-
777 niques in mineral exploration: In situ applications of x ray fluores-
778 cence techniques, final report of a coordinated research project 2000-
779 2003. Technical Report IAEA-TECDOC-1456, International Atomic En-
780 ergy Agency, 2005. URL `https://www.iaea.org/publications/7212/`
781 `in-situ-applications-of-x-ray-fluorescence-techniques`.

782 M. Lawrence-Snyder, J. Scaffidi, S. M. Angel, A. P. Michel, and A. D. Chave.
783 Laser-induced breakdown spectroscopy of high-pressure bulk aqueous solu-
784 tions. *Applied spectroscopy*, 60:786–790, 2006.

785 V. Lazic, F. Colao, R. Fantoni, and V. Spizzicchino. Laser-induced breakdown
786 spectroscopy in water: Improvement of the detection threshold by signal pro-
787 cessing. *Spectrochimica Acta Part B: Atomic Spectroscopy*, 60:1002–1013,
788 2005.

789 R. P. Lowell and M. DuBose. Hydrothermal systems on Europa. *Geophysical*
790 *Research Letters*, 32:1–4, 2005.

791 M. Z. Martin, M. A. Mayes, K. R. Heal, D. J. Brice, and S. D. Wullschleger. In-
792 vestigation of laser-induced breakdown spectroscopy and multivariate analysis
793 for differentiating inorganic and organic C in a variety of soils. *Spectrochimica*
794 *Acta Part B: Atomic Spectroscopy*, 87:100–107, 2013.

795 A. Matsumoto, A. Tamura, K. Fukami, Y. H. Ogata, and T. Sakka. Two-
796 dimensional space-resolved emission spectroscopy of laser ablation plasma in
797 water. *Journal of Applied Physics*, 113:053302, 2013.

798 A. Matsumoto, A. Tamura, R. Koda, K. Fukami, Y. H. Ogata, N. Nishi,
799 B. Thornton, and T. Sakka. On-Site Quantitative Elemental Analysis of
800 Metal Ions in Aqueous Solutions by Underwater Laser-Induced Breakdown
801 Spectroscopy Combined with Electrodeposition under Controlled Potential.
802 *Analytical Chemistry*, 87:1655–1661, 2015.

S. Maurice, S. M. Clegg, R. C. Wiens, O. Gasnault, W. Rapin, O. Forni, A. Cousin, V. Sautter, N. Mangold, L. Le Deit, M. Nachon, R. B. Anderson, N. L. Lanza, C. Fabre, V. Payré, J. Lasue, P.-Y. Meslin, R. J. Léveillé, B. L. Barraclough, P. Beck, S. C. Bender, G. Berger, J. C. Bridges, N. T. Bridges, G. Dromart, M. D. Dyar, R. Francis, J. Frydenvang, B. Gondet, B. L. Ehlmann, K. E. Herkenhoff, J. R. Johnson, Y. Langevin, M. B. Madsen, N. Melikechi, J.-L. Lacour, S. Le Mouélic, E. Lewin, H. E. Newsom, A. M. Ollila, P. Pinet, S. Schröder, J.-B. Sirven, R. L. Tokar, M. J. Toplis, C. D'Uston, D. T. Vaniman, and A. R. Vasavada. ChemCam activities and discoveries during the nominal mission of the Mars Science Laboratory in Gale crater, Mars. *Journal of Analytical Atomic Spectrometry*, 31:863–889, 2016.

A. P. M. Michel and A. D. Chave. Single pulse laser-induced breakdown spectroscopy of bulk aqueous solutions at oceanic pressures: interrelationship of gate delay and pulse energy. *Applied Optics*, 47:G122–G130, 2008.

A. P. M. Michel, M. Lawrence-Snyder, S. M. Angel, and A. D. Chave. Laser-induced breakdown spectroscopy of bulk aqueous solutions at oceanic pressures: evaluation of key measurement parameters. *Applied Optics*, 46:2507–2515, 2007.

K. A. Miller, K. F. Thompson, P. Johnston, and D. Santillo. An Overview of Seabed Mining Including the Current State of Development, Environmental Impacts, and Knowledge Gaps. *Frontiers in Marine Science*, 4, 2018.

Y. Nakajima, J. Yamamoto, T. Takahashi, B. Thornton, Y. Yamabe, G. Dodbiba, and T. Fujita. Development of elemental technologies for seafloor mineral processing of seafloor massive sulfides. In *Proceedings of Conference on Ocean, Offshore and Arctic Engineering,* OMAE2019-96040, Glasgow, Scotland, 2019.

T. Noguchi, R. Shinjo, M. Ito, J. Takada, and T. Oomori. Barite geochemistry from hydrothermal chimneys of the Okinawa Trough: insight into chimney

formation and fluid/sediment interaction. *Journal of Mineralogical and Petrological Sciences*, 106:26–35, 2011.

T. Nozaki, J.-I. Ishibashi, K. Shimada, T. Nagase, Y. Takaya, Y. Kato, S. Kawagucci, T. Watsuji, T. Shibuya, R. Yamada, T. Saruhashi, M. Kyo, and K. Takai. Rapid growth of mineral deposits at artificial seafloor hydrothermal vents. *Scientific reports*, 6:22163, 2016.

R. Nyga and W. Neu. Double-pulse technique for optical emission spectroscopy of ablation plasmas of samples in liquids. *Optical Letters*, 18:747–749, 1993.

A. Pichahchy, D. Cremers, and M. Ferris. Elemental analysis of metals under water using laser-induced breakdown spectroscopy. *Spectrochimica Acta Part B: Atomic Spectroscopy*, 52:25–39, 1997.

A. Purser, L. Thomsen, C. Barnes, M. Best, R. Chapman, M. Hofbauer, M. Menzel, and H. Wagner. Temporal and spatial benthic data collection via an internet operated Deep Sea Crawler. *Methods in Oceanography*, 5:1–18, 2013.

J. Rakovský, P. Čermák, O. Musset, and P. Veis. A review of the development of portable laser induced breakdown spectroscopy and its applications. *Spectrochimica Acta Part B: Atomic Spectroscopy*, 101:269–287, 2014.

M. Saeki, A. Iwanade, C. Ito, I. Wakaida, B. Thornton, T. Sakka, and H. Ohba. Development of a fiber-coupled laser-induced breakdown spectroscopy instrument for analysis of underwater debris in a nuclear reactor core. *Journal of Nuclear Science and Technology*, 51:930–938, 2014.

T. Sakka, H. Oguchi, S. Masai, K. Hirata, Y. H. Ogata, M. Saeki, and H. Ohba. Use of a long-duration ns pulse for efficient emission of spectral lines from the laser ablation plume in water. *Applied Physics Letters*, 88:061120, 2006.

T. Sakka, H. Oguchi, S. Masai, and Y. H. Ogata. Quasi Nondestructive Elemental Analysis of Solid Surface in Liquid by Long-pulse Laser Ablation Plume Spectroscopy. *Chemistry Letters*, 36:508–509, 2007.

T. Sakka, H. Yamagata, H. Oguchi, K. Fukami, and Y. H. Ogata. Emission spectroscopy of laser ablation plume: Composition analysis of a target in water. *Applied Surface Science*, 255:9576–9580, 2009.

T. Sakka, A. Tamura, A. Matsumoto, K. Fukami, N. Nishi, and B. Thornton. Effects of pulse width on nascent laser-induced bubbles for underwater laser-induced breakdown spectroscopy. *Spectrochimica Acta Part B: Atomic Spectroscopy*, 97:94–98, 2014.

B. Sallé, J.-L. Lacour, P. Mauchien, P. Fichet, S. Maurice, and G. Manhès. Comparative study of different methodologies for quantitative rock analysis by Laser-Induced Breakdown Spectroscopy in a simulated Martian atmosphere. *Spectrochimica Acta Part B: Atomic Spectroscopy*, 61:301–313, 2006.

J. B. Sirven, B. Bousquet, L. Canioni, and L. Sarger. Laser-induced breakdown spectroscopy of composite samples: Comparison of advanced chemometrics methods. *Analytical Chemistry*, 78:1462–1469, 2006.

P. Sobron, L. M. Barge, J. Amend, J. Burnett, R. Detry, I. Doloboff, D. S. Kelley, A. Marburg, A. K. Misra, A. Nawaz, R. E. Price, M. Smith, K. Zacny, and B. Thornton. Exploring underwater vent systems: New technologies and strategies to advance life detection and scientific understanding of ocean worlds. In *Fall Meeting 2018, abstract P33G-3903*. American Geophysical Union, 2018.

T. Takahashi, B. Thornton, and T. Ura. Investigation of Influence of Hydrostatic Pressure on Double-Pulse Laser-Induced Breakdown Spectroscopy for Detection of Cu and Zn in Submerged Solids. *Applied Physics Express*, 6: 042403, 2013.

T. Takahashi, B. Thornton, K. Ohki, and T. Sakka. Calibration-free analysis of immersed brass alloys using long-ns-duration pulse laser-induced breakdown spectroscopy with and without correction for nonstoichiometric ablation. *Spectrochimica Acta Part B: Atomic Spectroscopy*, 111:8–14, 2015.

T. Takahashi, B. Thornton, T. Sato, T. Ohki, K. Ohki, and T. Sakka. Temperature based segmentation of laser-induced plasmas for quantitative compositional analysis of brass alloys submerged in water. *Spectrochimica Acta Part B: Atomic Spectroscopy*, 124:87–93, 2016.

T. Takahashi, B. Thornton, T. Sato, T. Ohki, K. Ohki, and T. Sakka. Partial least squares regression calculation for quantitative analysis of metals submerged in water measured using laser-induced breakdown spectroscopy. *Applied Optics*, 57:5872–5883, 2018.

K. Takai, M. Mottl J., S. Nielsen H. H., and the IODP Expedition 331 Scientists. IODP expedition 331: Strong and expansive subseafloor hydrothermal activities in the Okinawa trough. *Science Reports*, 13:19–27, 2012.

B. Thornton. Sizing Drop Weights for Deep Diving Submersibles Taking Into Account Nonuniform Seawater Density Profiles. *IEEE Journal of Oceanic Engineering*, 2019. Accepted.

B. Thornton and T. Ura. Effects of Pressure on the Optical Emissions Observed from Solids Immersed in Water Using a Single Pulse Laser. *Applied Physics Express*, 4:022702, 2011.

B. Thornton, T. Sakka, T. Takahashi, A. Tamura, T. Masamura, and A. Matsumoto. Spectroscopic measurements of solids immersed in water at high pressure using a long-duration nanosecond laser pulse. *Applied Physics Express*, 6:082401, 2013a.

B. Thornton, T. Sakka, T. Takahashi, A. Tamura, A. Matsumoto, and T. Ura. Laser-induced breakdown spectroscopy for in situ chemical analysis at sea. In *Proceedings of 2013 IEEE International Underwater Technology Symposium (UT)*. IEEE, 2013b. URL `https://ieeexplore.ieee.org/abstract/document/6519823`.

B. Thornton, T. Sakka, T. Masamura, A. Tamura, T. Takahashi, and A. Matsumoto. Long-duration nano-second single pulse lasers for observation of

spectra from bulk liquids at high hydrostatic pressures. *Spectrochimica Acta Part B: Atomic Spectroscopy*, 97:7–12, 2014.

B. Thornton, T. Takahashi, T. Sato, T. Sakka, A. Tamura, A. Matsumoto, T. Nozaki, T. Ohki, and K. Ohki. Development of a deep-sea laser-induced breakdown spectrometer for in situ multi-element chemical analysis. *Deep-Sea Research Part I: Oceanographic Research Papers*, 95:20–36, 2015.

B. Thornton, A. Bodenmann, O. Pizarro, S. B. Williams, A. Friedman, R. Nakajima, K. Takai, K. Motoki, T. o Watsuji, H. Hirayama, Y. Matsui, H. Watanabe, and T. Ura. Biometric assessment of deep-sea vent megabenthic communities using multi-resolution 3d image reconstructions. *Deep-Sea Research Part I: Oceanographic Research Papers*, 116:200–219, 2016.

A. Whitehouse, J. Young, I. Botheroyd, S. Lawson, C. Evans, and J. Wright. Remote material analysis of nuclear power station steam generator tubes by laser-induced breakdown spectroscopy. *Spectrochimica Acta Part B: Atomic Spectroscopy*, 56:821–830, 2001.

R. C. Wiens, S. Maurice, B. Barraclough, M. Saccoccio, W. C. Barkley, J. F. Bell, S. Bender, J. Bernardin, D. Blaney, J. Blank, M. Bouyè, N. Bridges, N. Bultman, P. Caïs, R. C. Clanton, B. Clark, S. Clegg, A. Cousin, D. Cremers, A. Cros, L. DeFlores, D. Delapp, R. Dingler, C. D′Uston, M. Darby Dyar, T. Elliott, D. Enemark, C. Fabre, M. Flores, O. Forni, O. Gasnault, T. Hale, C. Hays, K. Herkenhoff, E. Kan, L. Kirkland, D. Kouach, D. Landis, Y. Langevin, N. Lanza, F. LaRocca, J. Lasue, J. Latino, D. Limonadi, C. Lindensmith, C. Little, N. Mangold, G. Manhes, P. Mauchien, C. McKay, E. Miller, J. Mooney, R. V. Morris, L. Morrison, T. Nelson, H. Newsom, A. Ollila, M. Ott, L. Pares, R. Perez, F. Poitrasson, C. Provost, J. W. Reiter, T. Roberts, F. Romero, V. Sautter, S. Salazar, J. J. Simmonds, R. Stiglich, S. Storms, N. Striebig, J.-J. Thocaven, T. Trujillo, M. Ulibarri, D. Vaniman, N. Warner, R. Waterbury, R. Whitaker, J. Witt, and B. Wong-Swanson. The ChemCam Instrument Suite on the Mars Science Laboratory (MSL) Rover:

944 Body Unit and Combined System Tests. *Space Science Reviews*, 170:167–227,
945 2012.

946 F. Yamamoto, T. Maki, T. Hyakudome, T. Sawa, S. Tsukioka, F. Saito,
947 A. Ishikawa, and K. Chiba. High-resolution bathymetric and geological sur-
948 vey of the iheya-north knoll, okinawa trough, using auv urashima. In *Abstract*
949 *of the 21st Meeting of the Japan Society for Marine Surveys and Technology*,
950 2009.

951 M. Yelameli, B. Thornton, T. Takahashi, T. Weerakoon, and K. Ishii. Classifi-
952 cation and statistical analysis of hydrothermal seafloor rocks measured under-
953 water using laser-induced breakdown spectroscopy. *Journal of Chemometrics*,
954 33:e3092, 2019.

955 S. Yoshino, B. Thornton, T. Takahashi, Y. Takaya, and T. Nozaki. Signal
956 preprocessing of deep-sea laser-induced plasma spectra for identi fi cation
957 of pelletized hydrothermal deposits using arti fi cial neural networks. *Spec-*
958 *trochimica Acta Part B: Atomic Spectroscopy*, 145:1–7, 2018.